

Development of a novel single-channel, 24 cm², SiPM-based, cryogenic photodetector

Marco D’Incecco, Cristiano Galbiati, Graham K. Giovanetti, George Korga, Xinran Li, Andrea Mandarano, Alessandro Razeto, Davide Sablone, and Claudio Savarese

Abstract—We report on the realization of a novel SiPM-based, cryogenic photosensor with an active area of 24 cm² that operates as a single-channel analog detector. The device is capable of single photon counting with a signal to noise ratio better than 13, a dark rate lower than 10⁻² cps/mm² and an overall photon detection efficiency significantly larger than traditional photomultiplier tubes. This development makes SiPM-based photosensors strong candidates for the next generation of dark matter and neutrino detectors, which will require multiple square meters of photosensitive area, low levels of intrinsic radioactivity and a limited number of detector channels.

Index Terms—SiPM arrays, large photodetectors, photon counting, cryo-electronics, low-noise electronics.

I. INTRODUCTION

The excellent single-photon resolution, photon detection efficiency, cryogenic performance and cost of silicon photomultipliers (SiPMs) makes them appealing replacements for conventional photomultiplier tubes in next generation physics experiments. However, SiPMs typically have active areas of several tens of square millimeters, meaning a large number of devices is required to instrument the area of a single photomultiplier tube. This poses significant space and interconnection challenges in large experiments, where readout cables are long and front-end electronics must be placed in close proximity to the detector. An extra layer of complication

Manuscript revisioned on November 6, 2017.

We acknowledge support from NSF (US, Grant PHY-1314507 for Princeton University), the Istituto Nazionale di Fisica Nucleare (Italy) and Laboratori Nazionali del Gran Sasso (Italy) of INFN.

Work at Princeton University was supported by Fermilab under Department of Energy contract DE-AC02-07CH11359.

M. D’Incecco is with INFN Laboratori Nazionali del Gran Sasso, Assergi (AQ) 67100, Italy.

C. Galbiati, G.K. Giovanetti and X. Li are with Physics Department, Princeton University, Princeton, NJ 08544, USA.

G. Korga is with Department of Physics, University of Houston, Houston, TX 77204, USA and INFN Laboratori Nazionali del Gran Sasso, Assergi (AQ) 67100, Italy.

A. Mandarano, and C. Savarese are with Gran Sasso Science Institute, L’Aquila 67100, Italy and INFN Laboratori Nazionali del Gran Sasso, Assergi (AQ) 67100, Italy.

D. Sablone and A. Razeto are with INFN Laboratori Nazionali del Gran Sasso, Assergi (AQ) 67100, Italy and Physics Department, Princeton University, Princeton, NJ 08544, USA.

Corresponding Author: sarlab7@lngs.infn.it

arises in rare-event searches, such as those searching for neutrinoless double-beta decay or dark matter, where the background contributions from cables and electronics are often dominant. One way to alleviate this problem is to group SiPMs together to reach a surface area equivalent to a photomultiplier tube and read them out as a single channel device. However, the high capacitance of SiPMs, about 50 pF/mm², makes it challenging to operate a large array of SiPMs as a single channel device while maintaining adequate timing resolution and single photon resolution.

A. Goals

This article focuses on the realization of a cryogenic, single analog output, SiPM-based photodetector with an active area comparable to a 3" photomultiplier tube (PMT) and better performance in terms of photon detection efficiency (PDE) and single photon resolution.

The SiPM layout and the front-end electronics have been designed to achieve a signal to noise ratio (SNR), defined here as the ratio between the amplitude of the single photo-electron signal and the standard deviation of the baseline noise, better than 10. At this noise level, the rate of baseline fluctuations misidentified as signals is well below the intrinsic dark rate of the SiPMs and the detector can operate as a single photon counter (see Section IV-D). In addition, the high bandwidth front-end electronics maintain the fast peak of the SiPM signals and allow for better than 20 ns timing resolution at 1 standard deviation. Finally, the overall power consumption of the front-end electronics is less than 250 mW, which avoids excessive heat dissipation into the detector’s cryogenic operating environment. This is comparable to the cryogenic PMTs used in the DarkSide-50 detector which dissipate around 100 mW plus an additional 90 mW from the cryogenic pre-amplifier [1].

B. Detector overview

The photodetector consists of 24 10 × 10 mm² SiPMs mounted on a substrate, referred to hereafter as a SiPM tile, mated to a board housing the front-end electronics. The 24 cm² SiPM tile is subdivided into 6 cm² quadrants

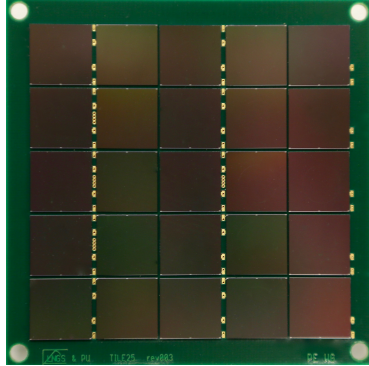


Fig. 1. Picture of the test SiPM tile described in the text (one SiPM is disconnected). For deployment in real detectors, the tile PCB would be re-designed to minimize any dead space, thereby increasing the overall photon detection efficiency.

and each quadrant is read out with an independent low-noise transimpedance amplifier (TIA) based on an LMH6629 high-speed operational amplifier [2]. The four TIA outputs are then summed by a second stage amplifier into a single analog output that is extracted from the cryogenic environment. The SiPM tile partitioning is driven by a compromise between a limit on the total power dissipation of the detector, equivalent to the total number of TIAs, and the bandwidth and SNR attainable for a given detector capacitance.

C. Cryogenic testing setup

The development and testing of the front-end electronics was done in a liquid nitrogen filled dewar with a flanged top. The dewar is sealed with a cover plate instrumented with a set of electrical and optical vacuum feedthroughs for power and signal lines and a calibration light source. A Keithley 2450 source measure unit was used for the SiPM bias voltage and a low-noise Elind 32DP8 power supply was used for the front-end amplifiers.

II. SiPM TILE

The SiPM tile is populated with $10 \times 10 \text{ mm}^2$ NUV-HD-LF SiPMs produced by Fondazione Bruno Kessler (FBK) for the DarkSide-20k collaboration [3]. NUV-HD SiPMs have a peak efficiency of about 40% in the near-ultraviolet, between 400–420 nm, and are fabricated with a cell border structure that allows for high-density packing of small cell sizes [4]. The low-field (LF) variant of NUV-HD SiPMs have a lower field in the avalanche region, reducing the field-enhanced dark count rate relative to standard field NUV-HD SiPMs [5]. The NUV-HD-LF devices used to fabricate the tile characterized in Section IV-D have $25 \mu\text{m}$ cells and $2.2 \text{ M}\Omega$ quenching resistors at room temperature. A comprehensive study of the performance of NUV-HD-LF SiPMs at cryogenic

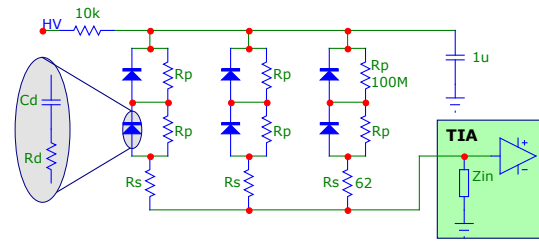


Fig. 2. Schematic of the SiPM layout for the 6 cm^2 tile quadrant.

temperature can be found in [6]: at 77 K and with 5 V of over-voltage, the darkrate is about $10 \times 10^{-3} \text{ cps/mm}^2$.

The SiPM parameters relevant to the design of the readout electronics are discussed in [7] and include the shape of the signal and the equivalent capacitance (C_d) and resistance (R_d) of the device. When operated in liquid nitrogen, $C_d = (4.2 \pm 0.1) \text{ nF}$ and $R_d = (61 \pm 1) \Omega$ for frequencies around 1 MHz. The value of R_d is negligible for frequencies above $\frac{1}{2\pi R_d C_d / 10}$ as described in [7].

SiPM dies are mounted on an FR4 printed circuit board (PCB) using EPO-TEK EJ2189-LV conductive, silver-loaded epoxy, which has been tested for mechanical and electrical stability after repeated thermal cycling in liquid nitrogen. The epoxy is screened onto the tile in a $60 \mu\text{m}$ thick layer, creating a coplanar surface on which the SiPM dice are placed with a manual die bonder. The top side pad of the SiPM is wedge bonded with aluminum wire to a trace on the PCB. The anode and cathode of each SiPM are routed to a high density Samtec LSS-150-01-L-DV-A connector on the back-side of the PCB that mates with the front-end board.

The SiPM tile is shown in Figure 1. Neglecting the tile border, which was used to ease handling during testing, the tile has a fill factor in excess of 90%, leading to an overall photon detection efficiency (PDE) at room temperature of about 35% [5]. This can be compared to a traditional 3" cryogenic Hamamatsu R11065 PMT, which has a quantum efficiency of 25% at room temperature and an active to total surface area ratio of 70% [8] (and the honeycomb packing loses an other 10%).

A. SiPM topology

In an ideal TIA, the overall noise is proportional to the square root of the detector capacitance, $\sqrt{C_d}$ ¹. In order to reduce the noise, the detector capacitance seen by the TIA can be limited by arranging the SiPMs in series. However, due to capacitive coupling between the SiPMs, the signal will also be attenuated by a factor equal to

¹This approximation is valid when the main contribution to the input equivalent noise is the voltage noise of the amplifier (e_n) and the other contributions (the current noise of the amplifier, i_n , and the Johnson-Nyquist noise of R_f) are negligible [9].

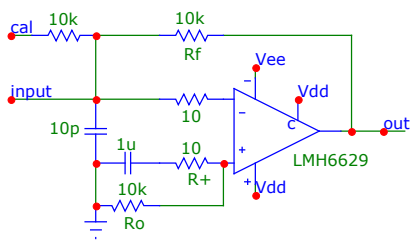


Fig. 3. Schematic of the trans-impedance amplifier used for the readout of the 6 cm² tile quadrant.

the number of SiPMs in series. Theoretically, these two effects balance one another and the SiPM configuration does not affect the SNR.

In practice, several effects come into play that change the theoretical balance in favour of the configuration shown in Figure 2 (3 branches with 2 SiPMs in series each). First, the input impedance of the TIA (Z_i) is non-zero. Therefore, a series resistance R_s limits losses toward the inactive branches of the quadrant (the branches with no detected light): the relative losses can be calculated equal to $\frac{Z_i}{Z_d + R_s/2}$, where Z_d is the complex impedance of the SiPM (which can be formulated in terms of R_d and C_d). This is particularly important for high frequencies, e.g., the initial discharge of the SiPM, where Z_i can be large and Z_d small. Second, R_s and R_d effectively limit the noise gain to $\frac{R_f}{(R_s + 2R_d)/3} + 1$, breaking the overall $\sqrt{C_d}$ noise dependence. Finally, the voltage noise at the TIA input includes the Johnson-Nyquist noise of R_d . Increasing the number of SiPMs in series reduces the signal and increases the noise, affecting the SNR.

The tile is subdivided into four quadrants of six SiPMs, each readout by an independent TIA with the configuration shown in Figure 2. This configuration optimizes the SNR and bandwidth when compared to alternative arrangements with the same surface area.

B. Bias voltage divider

At room temperature, the bias voltage across a series chain of SiPMs automatically equalizes due to the shared dark current between the devices [10]. The situation changes at cryogenic temperatures, where the SiPM dark rate drops below 0.1 Hz/mm². At a gain of about 1×10^6 , the dark current is only a few pA per device. In this regime, leakage currents dominate. The quiescent current flowing through the 10×10 mm² SiPMs was measured to be on the order of 0.2–1.5 nA.

To ensure even bias distribution between the series SiPMs, a resistor-based voltage divider is added to the circuit as shown in Figure 2. Three points are critical to the design of the divider:

- The precision of the divider has to compare with the desired gain uniformity (G_U) of the SiPMs. For

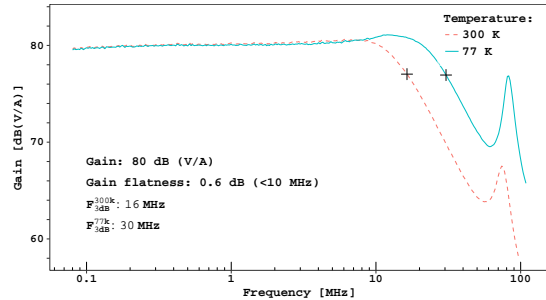


Fig. 4. Bode plot from an S_{21} scan of the TIA coupled to a 6 cm² SiPM tile quadrant at both room and liquid nitrogen temperature.

$G_U \geq 95\%$ and an over-voltage to bias ratio of about $\frac{5}{32}$, the voltage partitioning accuracy has to be better than 0.8%, which requires resistors with 0.5% tolerance.

- The current flowing through each voltage divider (i_d) has to be high enough so that a leakage current (i_l) from the SiPMs will not affect the voltage partitioning by more than the required gain uniformity. This is true when $i_d > i_l \frac{G_U}{2(1-G_U)}$. Assuming an upper limit on the leakage current at liquid nitrogen temperature of 20 nA, $i_d \geq 200$ nA.
- The shot noise of the total divider current ($3i_d$) can significantly contribute to the intrinsic noise of the amplifier. As described in [7], the current noise (i_n) of the LMH6629 at 77 K corresponds to the shot noise produced by a current of about 4 μ A. Therefore it is advisable to maintain $i_d \leq 1 \mu$ A.

The SiPM tile uses 1% tolerance, 100 M Ω resistors that were binned by their resistance at room temperature to improve the resistance variation within each divider to better than 0.5%.

III. 6 cm² ELECTRONICS

Each 6 cm² quadrant of the SiPM tile is readout by the TIA shown in Figure 3. This circuit is identical to the amplifier introduced in [7] with one relevant modification. The input bias current offset of the LMH6629 at cryogenic temperature depends strongly on the power supply voltage, see [7], which can cause low frequency noise and instability of the output offset. The standard solution to this problem is to match R_+ with R_f and add a bypass capacitor to filter the noise introduced by R_+ . However, this would reduce the effectiveness of R_+ at dumping oscillations. Therefore, R_+ is left untouched and an offset compensation resistor R_o equal in value to R_f is added along with a filter capacitor.

The gain and bandwidth of the TIA coupled with a 6 cm² SiPM tile quadrant are shown in Figure 4. The gain of the circuit is 80 dB(V/A), as expected with $R_f = 10$ k Ω , and a flatness of 0.6 dB up to 10 MHz. The bandwidth in liquid nitrogen is 30 MHz.

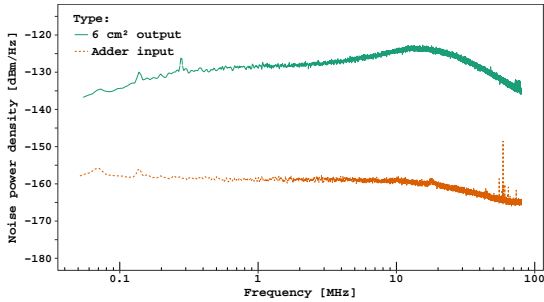


Fig. 5. Output noise spectral density of the 6 cm^2 quadrant described in the text and the input equivalent noise of the summing amplifier shown in Figure 9.

A. Noise model

The intrinsic voltage noise (ϵ_n) of the LMH6629 at 77 K is $0.3\text{ nV}/\sqrt{\text{Hz}}$, see [7]. The Johnson-Nyquist voltage noise from R_+ , $\frac{1}{3}R_s$ and $\frac{2}{3}R_d$ contribute an additional $\sim 0.5\text{ nV}/\sqrt{\text{Hz}}$, resulting in a total input voltage noise term $\sim 0.64\text{ nV}/\sqrt{\text{Hz}}$ (equivalent to -171 dBm). The voltage noise is amplified by the noise gain, which behaves like a high pass filter with $f_{3\text{dB}} \simeq \frac{1}{\pi(R_s+2R_d)C_d} \simeq 260\text{ kHz}$ and an asymptotic gain of $\frac{R_f}{(R_s+2R_d)/3} + 1 \simeq 165\text{ V/V}$ ($\sim 44\text{ dB}$). This should result in an output noise spectrum that plateaus above 1 MHz at -127 dBm .

At 77 K, the intrinsic current noise of the LMH6629 is $i_n = 1.3\text{ pA}/\sqrt{\text{Hz}}$ and the shot noise of the bias voltage divider, $3i_d$, is negligible. This results in an output noise density of $13\text{ nV}/\sqrt{\text{Hz}}$, corresponding to a flat spectrum at -145 dBm . The Johnson-Nyquist current noise of R_f in liquid nitrogen results in a second flat spectrum at -151 dBm . The sum of these two spectra in quadrature is -144 dBm . This current noise component only becomes significant below 10 kHz , where the output voltage noise drops by a few decades and, to first approximation, can be ignored.

Figure 5 shows the output noise spectrum of the TIA and 6 cm^2 SiPM tile quadrant measured with an R&S FSV-7 spectrum analyzer at 77 K. The features predicted by the model are present. The noise density at 1 MHz is -128 dBm and $f_{3\text{dB}} \simeq 200\text{ kHz}$. The peak at about 15 MHz in Figure 5 is not predicted by this simple noise model. The explanation of this peak is provided by the reduction of R_d at high frequencies as discussed in Section II.

B. Performance of the 6 cm^2 quadrant

The signal from the TIA once extracted from the dewar, is further processed at room temperature by a low-noise amplifier and then digitized by a 10 bit, 1 GS/s CAEN V1751 configured with a $5\text{ }\mu\text{s}$ pre-trigger and a $15\text{ }\mu\text{s}$ total gate time. The digitizer was triggered in coincidence with a light pulse from a Hamamatsu

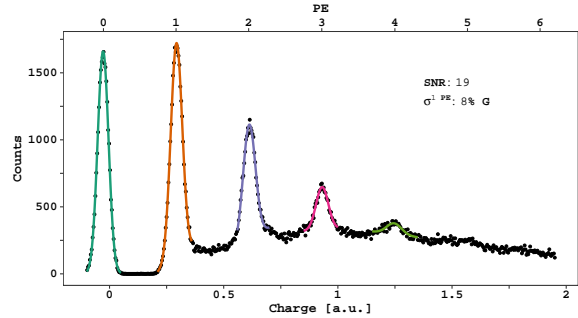


Fig. 6. Photoelectron spectrum from a 6 cm^2 detector quadrant calculated using a fixed window integration. The solid lines represent gaussian fits to the photoelectron and baseline peaks.

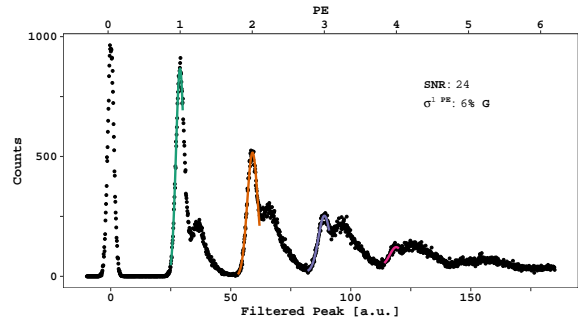


Fig. 7. Photoelectron spectrum of a 6 cm^2 detector quadrant calculated with a matched filter. The solid lines represent a gaussian fit to the low energy portion of the photoelectron peaks. The high energy tails of the peaks are distorted by events that contain an after-pulse.

PLP-10 sub-nanosecond 405 nm laser source. The output of the PLP-10 was attenuated so that an average of one photon was incident on the detector per pulse. The SiPMs were operated at an over-voltage of 5 V , corresponding to a gain of $1.5 \times 10^6\text{ C/C}$.

The amplitudes of the digitized waveforms were calculated offline using two different methods. Figure 6 shows the spectrum obtained using a fixed integration window of $2.2\text{ }\mu\text{s}$ (4τ). The baseline noise is 5% of the gain and the separation between the photoelectron peaks is limited by after-pulsing of the SiPMs. Figure 7 shows the spectrum obtained using a matched filter algorithm [11], which results in an SNR of 24. The matched filter more clearly separates events with after-pulses from the photoelectron peaks, resulting in non-gaussian peak shapes.

The gain uniformity of the first photoelectron peak in Figure 7 can be calculated by subtracting in quadrature the baseline noise from $\sigma_{1\text{PE}}$, resulting in $G_U = 96\%$, comparable to the specification outlined in Section II-B

IV. CRYOGENIC SUMMING AMPLIFIER

The output signals of the four TIAs from the four 6 cm^2 quadrants are combined at the input of a cryogenic summing amplifier that must amplify their sum for

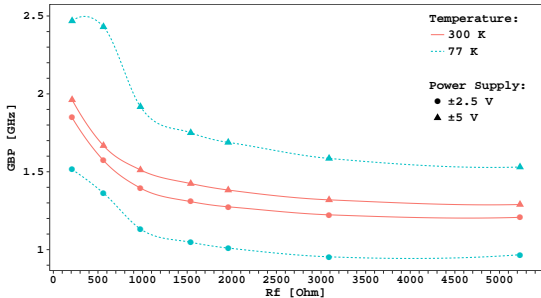


Fig. 8. Gain bandwidth product of the LMH6624 test circuit in the non-inverting configuration versus feedback resistor value at room temperature and in liquid nitrogen (gain = $R_f/25\Omega + 1$). The lines are drawn to guide the eye.

transmission across the dewar while maintaining the signal bandwidth, noise and dynamic range of the 6 cm^2 readout.

A. LMH6624 Cryogenic Characterization

The core of the summing amplifier is an LMH6624 operational amplifier from Texas Instruments. At room temperature, the LMH6624 has a gain bandwidth product of 1.5 GHz and an input voltage noise of $0.92\text{ nV}/\sqrt{\text{Hz}}$ [12]. The LMH6624 was characterized in a liquid nitrogen bath following the procedure described in [7]. The input voltage noise density at 77 K drops to $(0.53 \pm 0.02)\text{ nV}/\sqrt{\text{Hz}}$. Figure 8 shows the gain bandwidth product of the test circuit versus R_f . At room temperature, the change in the gain bandwidth product due to the power supply voltage is relatively small, while in liquid nitrogen the variation is almost a factor of two. The overall shape of the curves is due to stray capacitance in the feedback path. The 1 dB output compression point measured in liquid nitrogen is 2.2 and 5.8 V_{PP} (before back-termination) with a quiescent current of 3 and 5 mA respectively for ± 2.5 and ± 5 V power supplies.

B. Summing amplifier design

The summing circuit is shown in Figure 9. The input resistors (R_a) are 100Ω to avoid over-loading the LMH6629 output stage. The signal gain is 10 V/V and the noise gain is 41 [13]. The additional factor of ten amplification boosts the single photoelectron signal into the tens of millivolt range, simplifying the signal extraction and acquisition. The operational amplifier uses the same ± 2.5 V power supply as the TIAs.

The bandwidth of the circuit was measured with a Vector Network Analyzer (VNA) configured for S21 scan to be 36 MHz at room temperature and 30 MHz in liquid nitrogen. The electronic noise of the summing amplifier is dominated by the intrinsic voltage noise of the LMH6624 multiplied by the 41 V/V noise gain

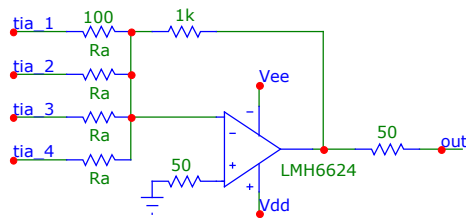


Fig. 9. Schematic of the summing amplifier used to combine the outputs of the SiPM tile quadrants.

and the Johnson-Nyquist noise of the input resistors. The overall input equivalent noise of the amplifier is $\frac{41}{10} \sqrt{(e_n^2 + 4k_B T \frac{R_a}{4})} f_{3dB} \frac{\pi}{2} \simeq 17\mu\text{V}$. Figure 5 compares the measured input equivalent noise spectrum of the amplifier to the output noise of the 6 cm^2 quadrant readout, demonstrating that the summing amplifier provides effectively no contribution to the overall noise of the system. In addition, the summing amplifier is slightly faster than the TIA and does not affect the bandwidth of the circuit. A 50Ω back-termination is added to avoid signal reflections on the coaxial cable: its net effect is a factor of two reduction in gain and electronic noise.

C. Offset and dynamic range

The coherent sum of the current through all of the bias voltage dividers can produce a considerable offset at the output of the summing amplifier, which can be evaluated as $12 i_d \times R_f \times 10/2$. In the present configuration, this becomes $+0.2\text{ V}$ after back-termination. Unfortunately, the amplified photoelectron signal is also positive (after two inversions) and the offset limits the dynamic range of the system to a few tens of photoelectrons. This was not a limitation for the present goal of performing low noise readout of a few photoelectrons. However, because offset contribution of the bias voltage divider is well known in advance, it is possible to bias the non-inverting pin of the amplifier and cancel the offset (or even further increase the negative offset). As an alternative, the authors are studying a rail to rail differential solution that would maximize the dynamic range.

D. Detector performance

The signal extraction from the summing amplifier, its digitization and the analysis algorithms follow the methods used for the 6 cm^2 detector described in Section III-B. The spectrum from the fixed window integration is shown in Figure 10 and the matched filter spectrum is shown in Figure 11. In both cases, the SNR is greater than 10 and the gain uniformity meets the design goal, $G_U = 95\%$.

The timing of an event can be extracted from the peak time of the matched filtered waveform, as described

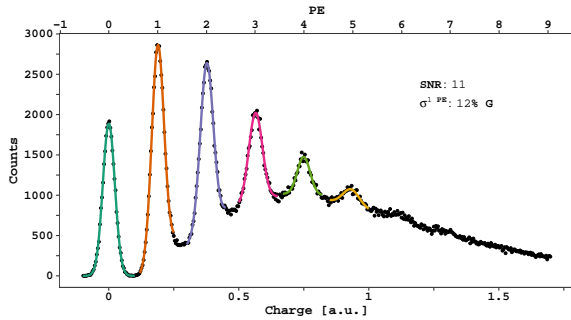


Fig. 10. Photoelectron spectrum of the full 24 cm^2 detector calculated using a fixed window integration. The solid lines represent a gaussian fit to the photoelectron and baseline peaks.

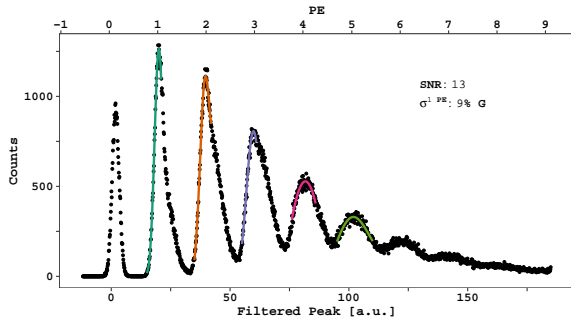


Fig. 11. Photoelectron spectrum of the full 24 cm^2 detector calculated using a matched filter. The solid lines represent a gaussian fit to the photoelectron peaks.

in [7]. Figure 12 shows the event amplitude versus the reconstructed event time. The distribution of the reconstructed arrival time of the single photoelectron peak (top panel of Figure 12) contains a narrow central peak, with a standard deviation of about 4 ns and non-gaussian tails that deteriorate the overall timing resolution to 16 ns. These tails account for less than 10% of the total events and are due to photoelectrons whose raw waveforms differ from the matched filter template. This is due to noise pickup jittering around the digitizer trigger, noise that, when coincident with the photoelectron signal, distorts the fast rising edge of the waveform and broaden the timing resolution.

V. CONCLUSIONS

We report on the first implementation of electronics for a large area (24 cm^2) single-channel, SiPM-based cryogenic photodetector with single photon sensitivity. This is achieved despite the large SiPM capacitance by subdividing the detector into four 6 cm^2 sub-arrays individually coupled to custom designed cryogenic transimpedance amplifiers. Signals from the four transimpedance amplifiers are then summed with a cryogenic summing amplifier to obtain a single-channel readout. Signals collected from the detector were analyzed using

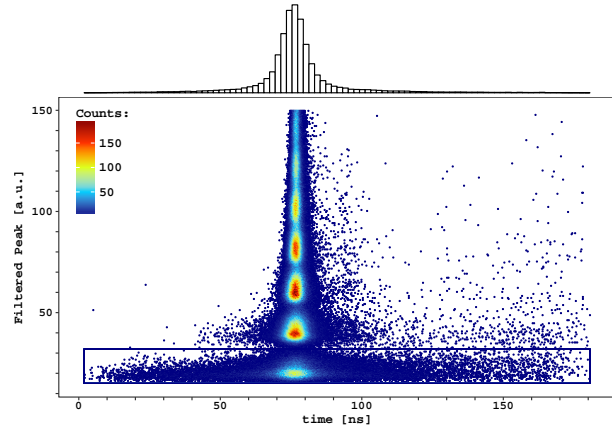


Fig. 12. Peak amplitude of the matched filtered waveform versus the reconstructed time relative to the laser sync. The top histogram shows the timing distribution of the single photoelectron peak (within the black box). The single photoelectron peak timing standard deviation is 16 ns.

a matched filtering technique, resulting in an excellent signal to noise ratio (>10) and timing resolution (<20 ns). Moreover, the excellent overall PDE ($\sim 35\%$) and very low dark rate (~ 24 cps) make these devices ideal candidates for future, low-background cryogenic dark matter and neutrino detectors.

REFERENCES

- [1] P. Agnes, I. F. M. Albuquerque, T. Alexander, A. K. Alton, K. Arisaka, D. M. Asner, M. Ave, H. O. Back, B. Baldin, K. Biery, V. Bocci, G. Bonfini, W. Bonivento, M. Bossa, B. Bottino, A. Brigatti, J. Brodsky, F. Budano, S. Bussino, M. Cadeddu, M. Cadoni, F. P. Calaprice, N. Canci, A. Candela, H. Cao, M. Caravati, M. Cariello, M. Carlini, S. Catalanotti, V. Cataudella, P. Cavalcante, A. Chepurinov, C. Cicalò, A. G. Cocco, G. Covone, L. Crippa, D. D'Angelo, M. D'Incecco, S. Davini, A. deCandia, S. DeCecco, M. DeDeo, G. DeFilippis, G. DeRosa, M. DeVincenzi, A. Derbin, A. Devoto, F. DiEusanio, C. Dionisi, G. DiPietro, E. Edkins, A. Empl, A. Fan, G. Fiorillo, K. Fomenko, G. Forster, D. Franco, F. Gabriele, C. Galbiati, S. Giagu, C. Giganti, G. K. Giovanetti, A. M. Goretti, F. Granato, L. Grandi, M. Gromov, M. Guan, Y. Guardincerri, B. R. Hackett, K. R. Herner, D. Hughes, P. Humble, E. V. Hungerford, A. Ianni, A. M. Ianni, I. James, T. N. Johnson, K. Keeter, C. L. Kendziora, V. V. Kobychev, G. Koh, D. Korabely, G. Korga, A. Kubankin, X. Li, M. Lissia, B. Loer, P. Lombardi, G. Longo, S. Luitz, Y. Ma, A. Machado, I. N. Machulin, A. Mandarano, S. M. Mari, J. Maricic, L. Marini, C. J. Martoff, P. D. Meyers, T. Miletic, R. Milincic, D. Montanari, A. Monte, M. Montuschi, M. E. Monzani, P. Mosteiro, B. J. Mount, V. N. Muratova, P. Musico, A. NavrerAgasson, A. Nelson, S. Odrowsk, A. Oleinik, M. Orsini, F. Ortica, L. Pagani, M. Pallavicini, E. Pantic, S. Parmeggiano, K. Pelczar, N. Pelliccia, A. Pocar, S. Pordes, D. A. Pugachev, H. Qian, K. Randle, G. Ranucci, M. Razeti, A. Razeto, B. Reinhold, A. L. Renshaw, M. Rescigno, Q. Riffard, A. Romani, B. Rossi, N. Rossi, S. D. Rountree, D. Sablone, P. Saggese, R. Saldanha, W. Sands, S. S. Sangiorgio, C. Savarese, B. Schlitzer, E. Segreto, D. A. Semenov, E. Shields, P. N. Singh, M. D. Skorokhvatov, O. Smirno, A. Sotnikov, C. Stanford, Y. Suvorov, R. Tartaglia, J. Tatarowicz, G. Testera, A. Tonazzo, P. Trinchese, E. V. Unzhakov, M. Verducci, A. Vishneva, R. B. Vogelaar, M. Wada, S. E. Walker, H. Wang, Y. Wang, A. W. Watson, S. Westerdale, M. M. Wojcik, X. Xiang, X. Xiao, J. Xu, C. Yang, J. Yoo, S. Zavatarelli, A. Zec, W. Zhong, C. Zhu,

- and G. Zuzel, "The Electronics, Trigger and Data Acquisition System for the Liquid Argon Time Projection Chamber of the DarkSide-50 Search for Dark Matter," *arXiv*, 2017. [Online]. Available: <http://arxiv.org/abs/1707.09889v1>
- [2] Texas Instruments, "LMH6629 Ultra-Low Noise, High-Speed Operational Amplifier with Shutdown," Texas Instruments, Tech. Rep., 2016. [Online]. Available: www.ti.com/lit/ds/symlink/lmh6629.pdf
- [3] C. E. Aalseth, F. Acerbi, P. Agnes, I. F. M. Albuquerque, T. Alexander, A. Alici, A. K. Alton, P. Antonioli, S. Arcelli, R. Ardito, I. J. Arndt, D. M. Asner, M. Ave, H. O. Back, A. I. B. Olmedo, G. Batignani, E. Bertoldo, S. Bettarini, M. G. Bisogni, V. Bocci, A. Bondar, G. Bonfini, W. Bonivento, M. Bossa, B. Bottino, M. G. Boulay, R. Bunker, S. Bussino, A. F. Buzulutskov, M. Cadeddu, M. Cadoni, A. Caminata, N. Canci, A. Candela, C. Cantini, M. Caravati, M. Cariello, M. Carlini, M. Carpinelli, A. Castellani, S. Catalanotti, V. Cataudella, P. Cavalcante, S. Cavuoti, R. Cereseto, A. Chepurinov, C. Cicalò, L. Cifarelli, M. Citterio, A. G. Cocco, M. Colocci, S. Corgioliu, G. Covone, P. Crivelli, I. D'Antone, M. D'Incecco, D. D'Urso, M. D. Da Rocha Rolo, M. Daniel, S. Davini, A. De Candia, S. De Cecco, M. De Deo, G. De Filippis, G. De Guido, G. De Rosa, G. Dellacasa, M. Della Valle, P. Demontis, A. Derbin, A. Devoto, F. Di Eusanio, G. Di Pietro, C. Dionisi, A. Dolgov, I. Dormia, S. Dussoni, A. Empl, M. F. Diaz, A. Ferri, C. Filip, G. Fiorillo, K. Fomenko, D. Franco, G. E. Froudakis, F. Gabriele, A. Gabrieli, C. Galbiati, P. G. Abia, A. Gendotti, A. Ghisi, S. Giagu, P. Giampa, G. Gibertoni, C. Giganti, M. A. Giorgi, G. K. Giovanetti, M. L. Gligan, A. Gola, O. Gorchakov, A. M. Goretti, F. Granato, M. Grassi, J. W. Grate, G. Y. Grigoriev, M. Gromov, M. Guan, M. B. B. Guerra, M. Guerzoni, M. Gulino, R. K. Haaland, A. Hallin, B. Harrop, E. W. Hoppe, S. Horikawa, B. Hosseini, D. Hughes, P. Humble, E. V. Hungerford, A. M. Ianni, C. Jillings, T. N. Johnson, K. Keeter, C. L. Kendziora, S. Kim, G. Koh, D. Korabely, G. Korga, A. Kubankin, M. Kuss, B. Lehnert, X. Li, M. Lissia, G. U. Lodi, B. Loer, G. Longo, P. Loverre, R. Lussana, L. Luzzi, Y. Ma, A. A. Machado, I. N. Machulin, A. Mandarano, L. Mapelli, M. Marcante, A. Margotti, S. M. Mari, M. Mariani, J. Maricic, C. J. Martoff, M. Mascia, M. Mayer, A. B. McDonald, A. Messina, P. D. Meyers, R. Milincic, A. Moggi, S. Moiola, J. Monroe, A. Monte, M. Morrocchi, B. J. Mount, W. Mu, V. N. Muratova, S. Murphy, P. Musico, R. Nania, A. N. Agasson, I. Nikulin, V. Nosov, A. O. Nozdrina, N. N. Nurakhov, A. Oleinik, V. Oleynikov, M. Orsini, F. Ortica, L. Pagani, M. Pallavicini, S. Palmas, L. Pandola, E. Pantic, E. Paoloni, G. Paternoster, V. Pavletcov, F. Pazzona, S. Peeters, K. Pelczar, L. A. Pellegrini, N. Pelliccia, F. Perotti, R. Perruzza, V. P. Fortes, C. Piemonte, F. Pilo, A. Pocar, T. Pollmann, D. Portaluppi, D. A. Pugachev, H. Qian, B. Radics, F. Raffaelli, F. Ragusa, M. Razeti, A. Razeto, V. Regazzoni, C. Regenfus, B. Reinhold, A. L. Renshaw, M. Rescigno, F. Retiere, Q. Riffard, A. Rivetti, S. Rizzardini, A. Romani, L. Romero, B. Rossi, N. Rossi, A. Rubbia, D. Sablone, P. Salatino, O. Samoylov, E. S. Garcia, W. Sands, M. Sant, R. Santorelli, C. Savarese, E. Scapparone, B. Schlitzer, G. Scioli, E. Segreto, A. Seifert, D. A. Semenov, A. Shchagin, L. Shekhtman, E. Shemyakina, A. Sheshukov, M. Simeone, P. N. Singh, P. Skensved, M. D. Skorokhvatov, O. Smirnov, G. Sobrero, A. Sokolov, A. Sotnikov, F. Speziale, R. Stainforth, C. Stanford, G. B. Suffritti, Y. Suvorov, R. Tartaglia, G. Testera, A. Tonazzo, A. Tosi, P. Trinchese, E. V. Unzhakov, A. Vacca, E. Vázquez-Jáuregui, M. Verducci, T. Viant, F. Villa, A. Vishneva, R. B. Vogelaar, M. Wada, J. Wahl, J. Walding, S. E. Walker, H. Wang, Y. Wang, A. W. Watson, S. Westerdale, R. Williams, M. M. Wojcik, S. Wu, X. Xiang, X. Xiao, C. Yang, Z. Ye, A. Y. de Llano, F. Zappa, G. Zappalà, C. Zhu, A. Zichichi, M. Zullo, and A. Zullo, "DarkSide-20: A 20 Tonne Two-Phase LAr TPC for Direct Dark Matter Detection at LNGS," *arXiv*, 2017. [Online]. Available: <http://arxiv.org/abs/1707.08145v1>
- [4] C. Piemonte, F. Acerbi, A. Ferri, A. Gola, G. Paternoster, V. Regazzoni, G. Zappala, and N. Zorzi, "Performance of NUV-HD Silicon Photomultiplier Technology," *IEEE Trans. Elec. Dev.*, vol. 63, no. 3, pp. 1111–1116, 2016. [Online]. Available: <http://ieeexplore.ieee.org/lpdocs/epic03/wrapper.htm?arnumber=7397984>
- [5] A. Ferri, F. Acerbi, A. Gola, G. Paternoster, C. Piemonte, and N. Zorzi, "Performance of FBK low-afterpulse NUV silicon photomultipliers for PET application," *JINST*, vol. 11, no. 03, pp. P03 023–P03 023, 2016. [Online]. Available: <http://stacks.iop.org/1748-0221/11/i=03/a=P03023?key=crossref.3b90668de68c0dbe8d723d4154a2ece8>
- [6] F. Acerbi, S. Davini, A. Ferri, C. Galbiati, G. Giovanetti, A. Gola, G. Korga, A. Mandarano, M. Marcante, G. Paternoster, C. Piemonte, A. Razeto, V. Regazzoni, D. Sablone, C. Savarese, G. Zappala, and N. Zorzi, "Cryogenic Characterization of FBK HD Near-UV Sensitive SiPMs," *IEEE Trans. Elec. Dev.*, pp. 1–6, 2017. [Online]. Available: <http://ieeexplore.ieee.org/document/7807295/>
- [7] M. D'Incecco, C. Galbiati, G. K. Giovanetti, G. Korga, X. Li, A. Mandarano, A. Razeto, D. Sablone, and C. Savarese, "Development of a very low-noise cryogenic pre-amplifier for large-area SiPM devices," *submitted to IEEE Transaction Nuclear Science*, 2017. [Online]. Available: <https://arxiv.org/abs/1706.04213>
- [8] Hamamatsu, "R11065-10 Photomultiplier Tube Datasheet," Hamamatsu, Tech. Rep., 2011.
- [9] Burr Brown, "Noise Analysis of FET Transimpedance Amplifiers," Texas Instruments, Tech. Rep. [Online]. Available: <http://www.ti.com/lit/an/sboa060/sboa060.pdf>
- [10] W. Ootani, "Development of pixelated scintillation detector for highly precise time measurement in MEG upgrade," *Nuclear Instruments and Methods in Physics Research Section A: Accelerators, Spectrometers, Detectors and Associated Equipment*, vol. 732, pp. 146 – 150, 2013, doi: 10.1016/j.nima.2013.07.043. [Online]. Available: <http://www.sciencedirect.com/science/article/pii/S0168900213010528>
- [11] G. Turin, "An introduction to matched filters," *IEEE Trans. Inform. Theory*, vol. 6, no. 3, pp. 311–329, 1960. [Online]. Available: <http://ieeexplore.ieee.org/document/1057571/>
- [12] Texas Instruments, "LMH6624 and LMH6626 Single/Dual Ultra Low Noise Wideband Operational Amplifier," Texas Instruments, Tech. Rep., 2014. [Online]. Available: <http://www.ti.com/lit/ds/symlink/lmh6624.pdf>
- [13] Analog Devices, "Op Amp Bandwidth and Bandwidth Flatness," Analog Devices, Tech. Rep. [Online]. Available: <http://www.analog.com/media/en/training-seminars/tutorials/MT-045.pdf>